Chemistry & Biology
Resource

Morphobase, an Encyclopedic Cell Morphology Database, and Its Use for Drug Target Identification

Yushi Futamura,[1,3] Makoto Kawatani,[1,3] Sayaka Kazami,[1] Kenichi Tanaka,[1] Makoto Muroi,[1] Takeshi Shimizu,[1] Koji Tomita,[1,2] Nobumoto Watanabe,[1] and Hiroyuki Osada[1,2,*]
[1]Chemical Biology Core Facility, Chemical Biology Department, RIKEN Advanced Science Institute, Wako-shi, Saitama 351-0198, Japan
[2]Graduate School of Biomedical Sciences, Tokyo Medical and Dental University, Tokyo 113-8510, Japan
[3]These authors contributed equally to this work
*Correspondence: hisyo@riken.jp
http://dx.doi.org/10.1016/j.chembiol.2012.10.014

SUMMARY

Visual observation is a powerful approach for screening bioactive compounds that can facilitate the discovery of attractive druggable targets following their chemicobiological validation. So far, many high-content approaches, using sophisticated imaging technology and bioinformatics, have been developed. In our study, we aimed to develop a simpler method that focuses on intact cell images because we found that dynamic changes in morphology are informative, often reflecting the mechanism of action of a drug. Here, we constructed a chemical-genetic phenotype profiling system, based on the high-content cell morphology database Morphobase. This database compiles the phenotypes of cancer cell lines that are induced by hundreds of reference compounds, wherein those of well-characterized anticancer drugs are classified by mode of action. Furthermore, we demonstrate the applicability of this system in identifying NPD6689, NPD8617, and NPD8969 as tubulin inhibitors.

INTRODUCTION

With the completion of the sequencing of the human genome and the demonstration of dramatic clinical efficacy for emerging molecular-target drugs, particularly imatinib, the trend in anticancer drug discovery has shifted to a molecular target-based approach. Whereas target-based screenings are believed to be the most rational and powerful, classical phenotype screenings, such as morphology-based assay, have been reconsidered and reintroduced as a complementary strategy for drug discovery, especially in the exploration of first-in-class therapeutics. For instance, certain benzoquinone ansamycins, such as herbimycin and geldanamycin, were found to revert tyrosine kinase-dependent oncogenic transformation (Uehara et al., 1986), the molecular target of which Whitesell et al. (1994) identified as HSP90. Similarly, lactacystin, discovered as an inducer of differentiation in Neuro2A cells, was demonstrated to target the 20S proteasome, indicating that proteasome inhibitors generally have selective anticancer activity (Fenteany et al., 1995; Omura et al., 1991).

Accordingly, phenotype-based screens are yet recognized as a new method of drug discovery, and newly modified phenotypic screens such as high-throughput, high-content imaging-driven, and omics-based screens have been developed as the initial step in the discovery of small molecule probes and drugs (Feng et al., 2009; Houle et al., 2010; Roti and Stegmaier, 2012). With this renewed interest in phenotype screens, however, the deduction of a molecular target of putative hits still remains the rate-limiting stage, despite the significant technological advances in chemical biology. The success rate of identifying a compound with a specific mechanism of action and its efficacy depends on our ability to compile and analyze the knowledge of the possible molecular targets related to phenotypes. In this regard, a multidimensional cell-based phenotype profiling approach that is supported by genetic modification, e.g., genome-wide gene depletion (genetics) or the application of well-validated chemotherapeutics (chemical genetics), can offer a promising strategy for discovering new drugs and defining their mechanisms of action. This strategy has allowed us and other groups to establish such profiling systems and report many important findings in recent years. For example, Perlman et al. (2004) presented a high-throughput cytological profiling method, in which the effects of 100 compounds were examined at 13 3-fold dilution of each drug on various cellular components in HeLa cells. To assess the similarity of compounds, they integrated a titration-invariant similarity score to succeed in grouping compounds with similarly reported targets and classifying a poorly characterized austocystin to transcription and translation inhibitors (Perlman et al., 2004). The CalMorph system, developed by Ohya and colleagues, which compiled comprehensive yeast cell morphological profiles of 4,718 nonessential gene deletion mutants, deduced the cellular functions of well-characterized drugs by comparing the morphological changes that were induced by gene deletion and versus the test compound (Ohnuki et al., 2010). Abassi et al. (2009) developed a cell-based kinetic profiling approach using impedance readout to monitor the effects of approximately 260 small molecules. This approach has been used to analyze the calcium-modulating activity of celecoxib, a Cox2 inhibitor, and identify an additional mechanism (calcium channel inhibitory activity) for the Eg5 inhibitor, monastrol (Abassi et al., 2009). Similarly,

Westwick group performed high-content protein-fragment complementation assays to measure changes in protein complexes in response to 107 drugs, characterizing the off-target effects and hidden phenotypes of certain drugs (MacDonald et al., 2006). Recently, we reported a proteome-based profiling system to predict the mechanism of action and molecular target of a compound of interest (Muroi et al., 2010) and demonstrated that BNS22 targets the catalytic domain of DNA topoisomerase II (TOP2). This new type of TOP2 inhibitor is an attractive chemotherapeutic agent as an alternative to topoisomerase poisons such as etoposide (Kawatani et al., 2011).

Even so, a primary screening is merely the starting point, and one must challenge how to exploit unique bioactive substances from a huge library rapidly and simply. To this end, we propose chemical-genetic cell morphological profiling as a promising method. The characteristic changes in morphology on exposure to an agent are often associated with its mechanism of action. Moreover, our data indicate that intact morphological changes alone—without excessive immunological or fluorescent staining—are sufficient to profile drug responses (Osada et al., 1988, 1997). In this study, using two cancer cell lines, we constructed an encyclopedia of cellular morphology, Morphobase, consisting of the cell shape changes induced by various compounds. Specifically, we developed a high-content image analysis method to examine the effects of approximately 200 routinely used chemicals on morphology, accompanied by statistical characterization of the obtained phenotypic data. The importance of this database was verified by its identification of the mechanism of action of three candidate drugs, comparing the similarity in morphological features by test compounds and those in the training data set. The Morphobase strategy not only reproduces "drug-target-phenotype" relationships for drugs with known targets, it also predicts unreported mechanisms of action and facilitates the discovery of novel drug candidates.

RESULTS

Tumor Cells Undergo Dynamic Changes Related to the Mode of Action of a Drug

To construct the cell morphology database, we examined the effects of roughly 30 well-characterized drugs on cell shape in two mammalian cell lines—the human cervix epidermoid carcinoma cell line HeLa and rat kidney cells that were infected with ts25, a T class mutant of Rous sarcoma virus Prague strain, *src*^{ts}-NRK cells—over time and by dose. As summarized in Figures 1 and S1A (available online), the cells that were exposed to an agent underwent typical morphological changes, which were similar between compounds of a pharmacological class. For instance, protein synthesis inhibitors, such as reveromycin A, cycloheximide, and anisomycin, induced the reversion of the spherical shape of transformed *src*^{ts}-NRK cells to a flattened shape, characteristic of normal cells (Takahashi et al., 1992). The morphological changes in *src*^{ts}-NRK cells were classified roughly into three categories—(1) flattened, (2) polygonal, and (3) rounded—and subgrouped by variation in size and the presence of unique granular structures, spikes, and vacuoles (Figure S1B). In contrast, the morphological changes in HeLa cells were less complicated, falling into three broad classes: (1) flattened, (2) round up, and (3) toxic/growth inhibition, which usually reflect stages in the cell cycle (G1/S phase, flattened with embossed nucleus; G2/M, round up). These preliminary observations indicated that the data on one cell line were not sufficient to characterize each therapeutic group of anticancer agents. However, the phenotypic response data of two or more distinct cell lines can discriminate features that are related to the mechanism of action of a particular compound.

High-Content Image Analysis of Subtle and Complex Changes in Morphology

To eliminate unintentional human errors during visual inspection, we recorded morphological changes using an automatic system, the IN Cell Analyzer, to perform a high-content image analysis. This system can automatically recognize cytoskeletal morphology and subcellular components and systematically generate quantitative morphological data.

To manage the vast variety of phenotypes that are induced by mechanistically distinct compounds, a custom-made image analysis algorithm was designed using IN Cell Developer Toolbox (GE Healthcare). On the first attempt, bright-field cell images were collected by the IN Cell Analyzer, but it appeared to be difficult to define every single cell accurately. Thus, nuclear staining with Hoechst 33342 was introduced to define the boundary between the cells and background. The unique textures that were induced by a drug on the cell surface or inside the cell were defined by the descriptor termed "Granular" for the segmentation of these components (see Figure 2A and Experimental Procedures for detailed segmentation algorithm). Using this method, various types of morphological changes in *src*^{ts}-NRK and HeLa cells that were induced by small molecules—the sizes and shapes, either of single cell or even tightly packed cells—could be successfully segmented from one another, confirming that this general cellular segmentation algorithm can monitor complex phenotypic responses in relevant cancer cell types (Figure 2B). Figure 2C shows the flowchart of image processing and measurements of morphological parameters for the next data mining step. Once the bright-field and Hoechst images of *src*^{ts}-NRK or HeLa cells that were exposed to various drugs were acquired, the "Nuclear," "Cell," and "Granular" fragments were properly segmented, and 12 morphological parameters were output automatically.

Statistical Analysis of Multiparametric Phenotype Data and Classification by Mode of Action

A test set of 207 authentic compounds, supplied by the RIKEN Natural Products Depository (NPDepo) (http://www.npd.riken.jp/npd) and SCADS inhibitor kits, was created (Table S1). Of these compounds, 54 were drugs with well-characterized mechanisms of action, 118 were commonly used experimental drugs, 26 were FDA-approved drugs, 7 were reported to have multiple biological targets, and 2 were antibiotics. To standardize the conditions for monitoring the resulting morphological changes, the following growth inhibitory concentrations were used: $IC_{85–95}$ values for HeLa cells and $IC_{50–60}$ for *src*^{ts}-NRK cells, calculated after a 48 hr exposure. The corresponding data are shown in Table S1. For compounds with low cytotoxicity, a maximum concentration of 25 μM was chosen for the exposure. Following incubation, cells were fixed and stained with

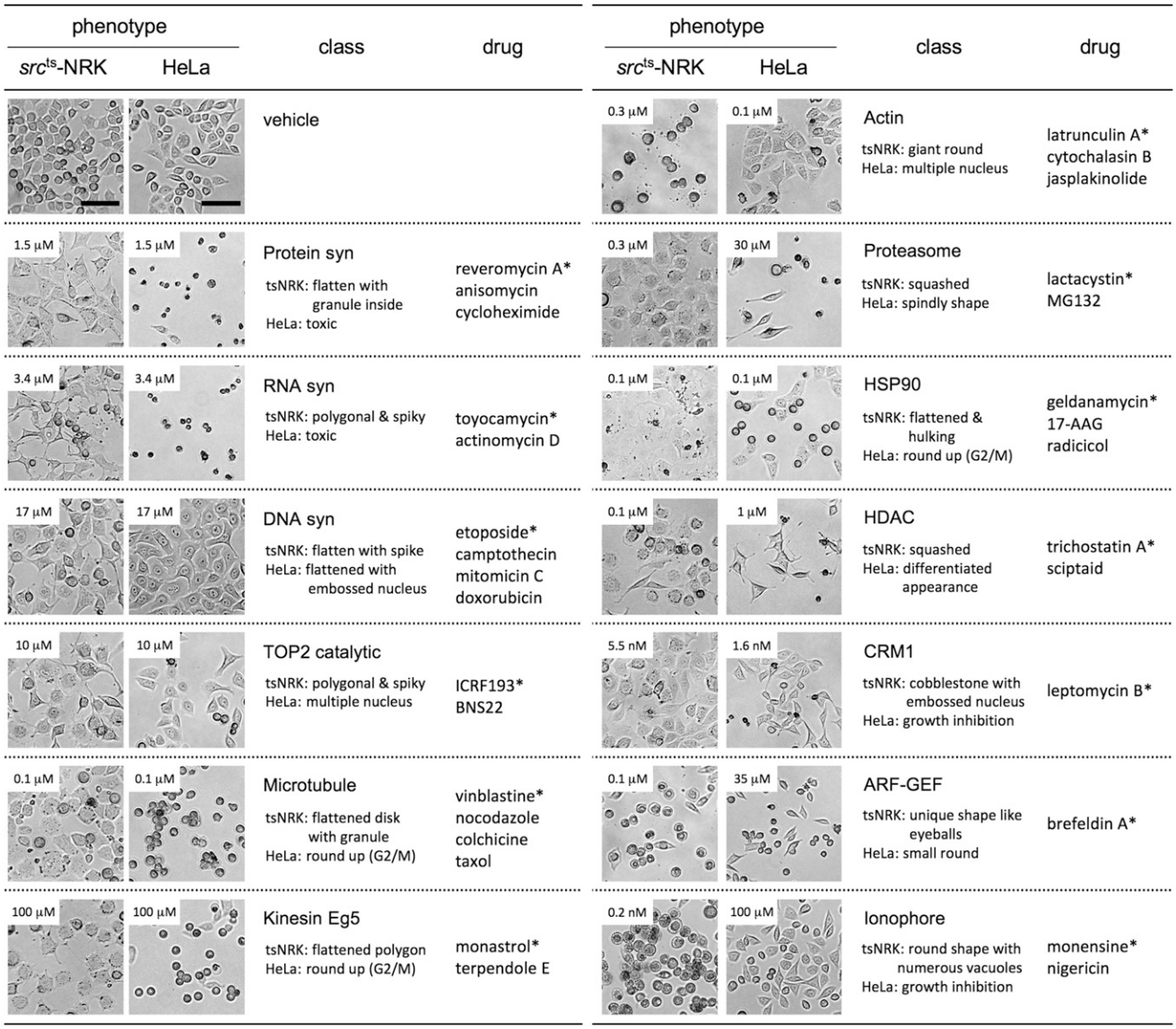

Figure 1. A Variety of Cell Shape Changes in *src*^{ts}-NRK Cells Induced by Well-Characterized Drugs Classified by Mode of Action

src^{ts}-NRK and HeLa cells were treated with well-characterized drugs at various concentrations and times. Representative images are shown of morphological changes of *src*^{ts}-NRK cells and HeLa cells observed under a microscope at 48 and 24 hr after treatment of a drug marked by an asterisk (*). Scale bars, 100 μm. See also Figure S1.

Hoechst 33342 to visualize the nuclei. Using IN Cell Analyzer, images of up to 1,500 cells from each well were collected and analyzed using the image segmentation procedures above. A set of descriptors, such as "Nuclear," "Cell," and "Granule," was applied to each cell. To characterize "well-level" responses, each parametric measurement was averaged, and the median and SD were calculated to account for bi- or polyphasic phenotype responses, such as a mixture of large and small cells (Figure 3). In total, 71 parameters were identified from 24 descriptors, yielding 14,697 data points (71 parameters × 207 compounds).

To analyze this amount of multiparametric data, we developed a data analysis program that incorporates multivariate statistical tools to automatically analyze, visualize, and rank multiparametric high-content phenotype results. Principal component analysis (PCA) was applied to visualize the multiparametric phenotype responses, and morphological similarities were defined using our original index, termed "probability scores" and Euclidean distance (Figure 3). Figure 4 shows the projection of the samples' PCA scores onto the first two principal components, which explains approximately 50% of variation in the data set. The black dots in the middle represent the group of vehicle controls; other spots on the 2D scatterplots represent individual compounds, and the points of well-characterized drugs are colored by target based on the literature. As a result, drugs that had similar activities formed a cluster: the drugs with a similar effect were circled by the same dotted lines, wherein specific phenotypic responses were shown as distinct

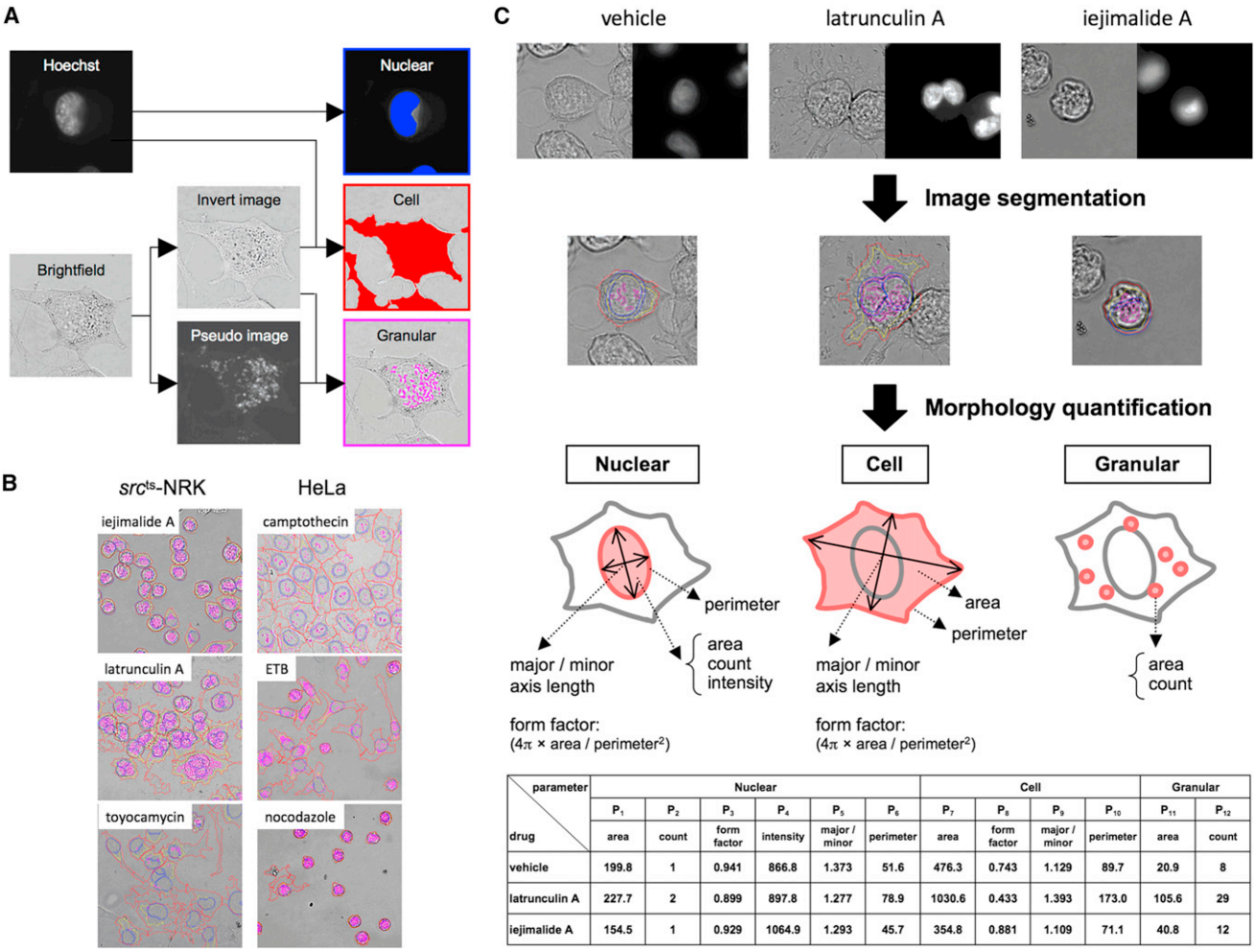

parameter / drug	Nuclear						Cell				Granular	
	P_1	P_2	P_3	P_4	P_5	P_6	P_7	P_8	P_9	P_{10}	P_{11}	P_{12}
	area	count	form factor	intensity	major / minor	perimeter	area	form factor	major / minor	perimeter	area	count
vehicle	199.8	1	0.941	866.8	1.373	51.6	476.3	0.743	1.129	89.7	20.9	8
latrunculin A	227.7	2	0.899	897.8	1.277	78.9	1030.6	0.433	1.393	173.0	105.6	29
iejimalide A	154.5	1	0.929	1064.9	1.293	45.7	354.8	0.881	1.109	71.1	40.8	12

Figure 2. Flowchart of Image Processing and Quantification of Morphological Parameters

(A) Scheme of the image segmentation program. The input images of bright-field and the same Hoechst 33342-stained cells were used for "Nuclear," "Cell," and "Granular" segmentation. "Nuclear" (blue) was assigned a nuclear-stained image. "Cell" (red) segmentation was achieved by allocating "Cell center," derived from the inverted bright-field image and nuclear information. "Granular" (pink) was defined based on inverted and pseudofluorescence bright-field images.

(B) Representative examples of the broad spectrum of heterogenic phenotype captures induced by distinct compounds. Nuclear and Cell region are colored in blue and red, respectively. The pink bullets show Granular structures, and the yellow lines show Cell center.

(C) Scheme of image processing and morphology parameter measurement. After *src*^{ts}-NRK or HeLa cells were segmented, 12 morphological parameters (P1–P12) were quantified for each cell.

See also Table S1.

distributions in the scatterplots. For instance, when we ranked the nearest neighbors to every tubulin-targeted compound by similarity, as determined by Euclidean distance metrics, typical microtubule inhibitors nearly always ranked in the top 20 (Figure 4; Table S2). Similarly, other inhibitors with typical modes of action, such as macromolecular synthesis, HDAC, and HSP, were also well classified (Table S2), suggesting that our high-content system can be successful in profiling phenotypes by drug function and in a copy mimicking the visual observation.

In this system, given that test compounds form a cluster with certain reference drugs of the data set, they are likely to have similar or identical cellular targets. We chose a well-characterized drug set, comprising 54 drugs with 14 molecular targets (Table S1), to encompass common mechanisms of toxicity and therapeutic actions against cancer cells. Then, we developed a training algorithm that determines which of the 14 target class in the training set were plausible candidates for compounds of interest by "probability scores," the mean Z scores for a test compound to the median point of each target class (see Experimental Procedures).

We employed three bioactive compounds (rotenone, 3-ATA, resveratrol) to evaluate our proposed method. Rotenone is a specific inhibitor of mitochondrial complex I, and 3-ATA was developed as a CDK4 kinase inhibitor in vitro (Kubo et al., 1999). Resveratrol has multiple activities, such as antioxidant, anti-inflammatory, and anticancer properties (Frémont, 2000). These compounds were tested in a newly established cell morphology system and primarily expressed two characteristics (Figure 5A). The high-content image profiling suggested that rotenone was significantly associated with the tubulin cluster

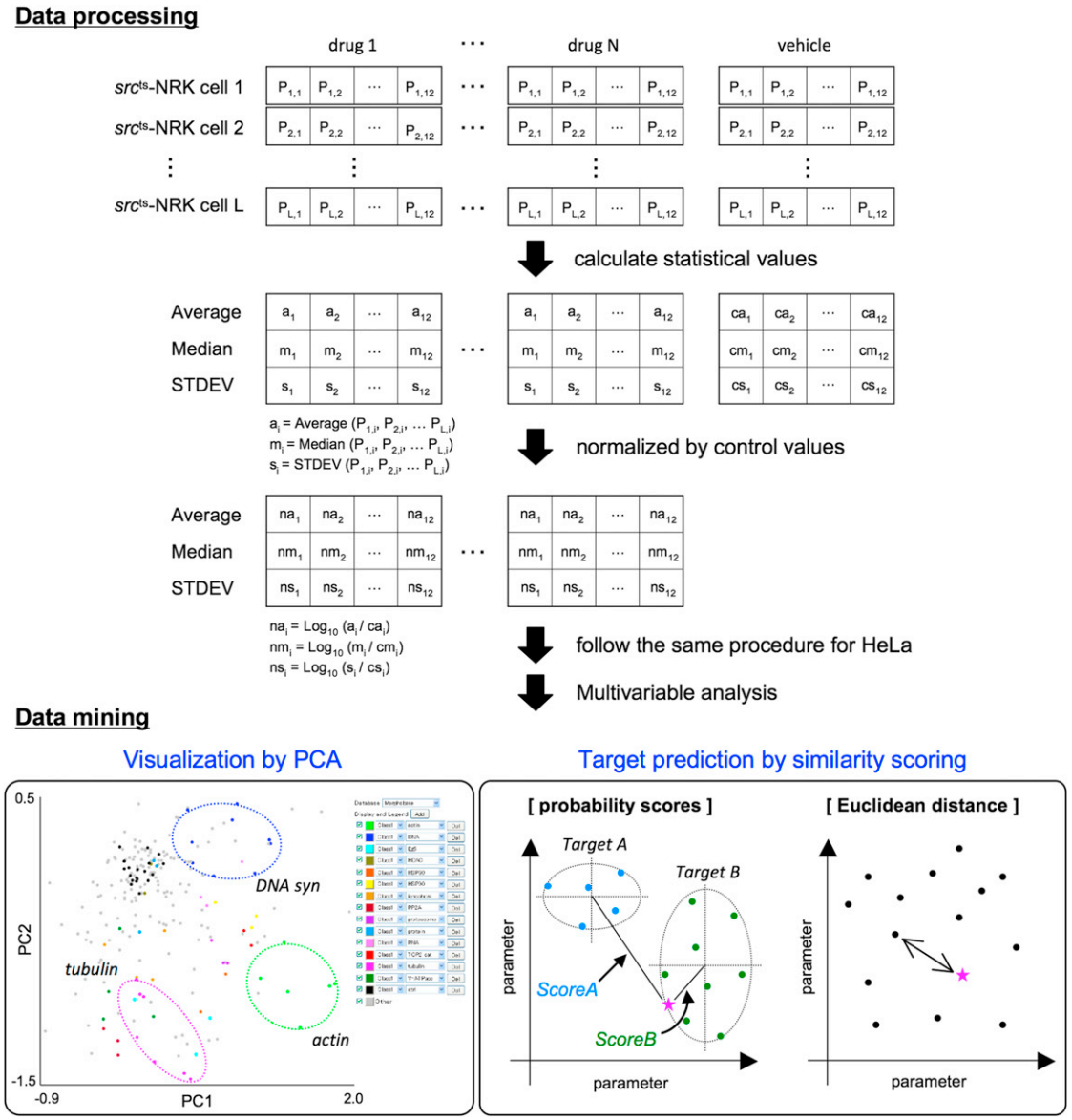

Figure 3. Schematic of Data Processing and Data Mining Step

Statistical values (Average, Median, SD) of obtained morphological parameters for ~1,000 drug N-treated *src*^{ts}-NRK and HeLa cells were calculated and normalized to the control average values as drug N-specific phenotypic multiparameters. Phenotypic multiparameters of 207 test compounds profiled by multivariate statistical analysis are illustrated. Morphobase profiling results are visualized by PCA, and the similarities in morphological changes between a compound of interest and reference compounds are defined using two statistical computations. See also Table S1.

($Score_{tubulin}$ = 1.03) and that 3-ATA and resveratrol were associated with the inhibitors of DNA synthesis ($Score_{DNA}$ = 1.56 and 0.92, respectively), based on probability scores (Figure 5B) and the rank of the top 20 nearest neighbors (Table S3). Actually, these compounds also induce other effects that are unrelated to the primary targets. Rotenone is an effective mitotic agent (Brinkley et al., 1974), 3-ATA affects DNA synthesis in an intact cell system (Diccianni et al., 2004), and most recent literature described that resveratrol acts as a TOP2 poison in cancer cells (Leone et al., 2010). Morphobase mostly provided the responsible target for the growth inhibition and deduced their reported side effects in the aforementioned case, indicating that our profiling approach detects the targets of drug candidates and determines their mechanisms of action.

Target Prediction of Compounds of Interest by Morphobase Profiling

Through our phenotypic screening of a chemical library in NPDepo, we identified several hundreds of compounds that inhibited the growth of the human promyelocytic leukemia cell line HL-60. In particular, NPD6689, NPD8617, and NPD8969 were very potent, as evidenced by the nanomolar ranges of their IC_{50} values (Table 1). By cell-cycle analysis of HeLa cells that were exposed to NPD6689 for 24 hr, the population in G2/M

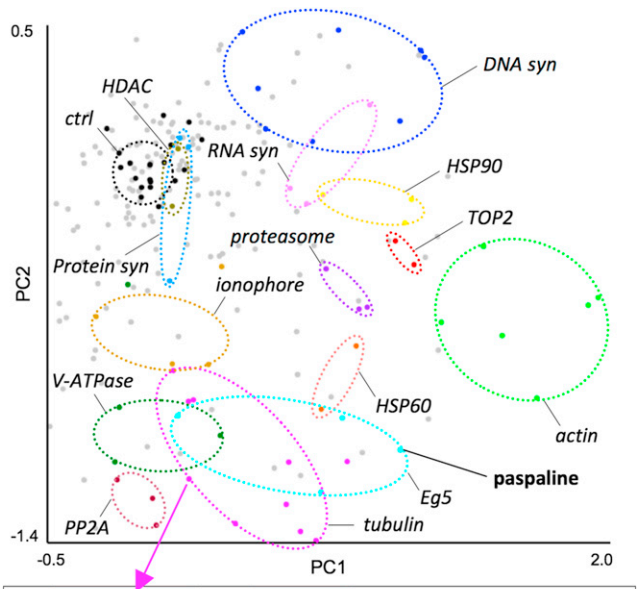

Sample podophyllotoxin Database Morphobase

Class Rank	Class	Score
1	tubulin	0.71
2	ionophore	2.31
3	PP2A	2.54
4	Eg5	2.74
5	DNA	2.94
6	V-ATPase	3.09
7	actin	3.88
8	HSP60	3.94
9	RNA	4.17
10	HSP90	4.44
11	proteasome	5.55
12	HDAC	5.91
13	ctrl	6.00
14	protein	7.85
15	TOP2 cat	11.29

Sample Rank	Sample	Class	Target	MOA	Distance
1	podophyllotoxin	tubulin	tubulin	microtubule dynamics	0.00
2	colchicine	tubulin	tubulin	microtubule dynamics	0.63
3	nocodazole	tubulin	tubulin	microtubule dynamics	0.83
4	SB225002		CXCR2	chemokine receptor	0.84
5	benomyl	tubulin	tubulin	microtubule dynamics	0.85
6	vinblastine	tubulin	tubulin	microtubule dynamics	0.89
7	monensin	ionophore	Na+	vesicle trafficking	0.90
8	Aurora inhibitor III		Aurora A	mitotic kinase	0.92
9	NPD8617		tubulin	microtubule dynamics	0.94
10	cantharidin	PP2A	PP1/PP2A	phosphatase	0.95
11	NPD6689		tubulin	microtubule dynamics	0.97
12	okadaic acid	PP2A	PP1/PP2A	phosphatase	0.97
13	concanamycin A	V-ATPase	V-ATPase	vesicle trafficking	0.97
14	rotenone		complex I, tubulin	mitochondria respiration	0.98
15	toutomycin	PP2A	PP1/PP2A	phosphatase	0.99
16	indirubin-3′-monoxime		GSK3b	GSK3b	1.00
17	PDGFR inhibitor IV		PDGFR	RTK	1.02
18	paclitaxel	tubulin	tubulin	microtubule dynamics	1.02
19	ATM/ATR kinase inhibitor		ATM	ATM	1.02
20	zGLFGMK		cathepsin G	peptidase	1.04

Figure 4. Overview of Morphobase Profiling

The user interface displays the results of principle component scores in a 2D scatterplot. The well-defined clusters can be distinguished from others by their mechanisms of action. It also displays the compound's predicted mode of action and its probability score: smaller scores reflect higher probabilities. It next ranks the 20 nearest neighbors of a test compound based on the Euclidean distance between the selected compound's positions. ctrl, control; syn, synthesis. See also Figures S5 and S6 and Tables S1 and S2.

A

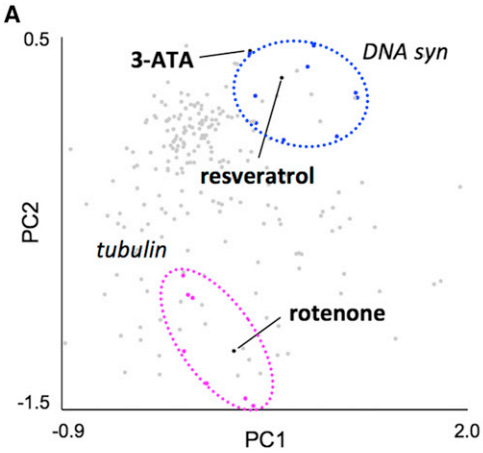

B

Rotenone Rank	Class	Score
1	tubulin	1.03
2	Eg5	1.92
3	HSP60	2.13
4	ionophore	2.26
5	V-ATPase	2.72
6	actin	2.87
7	DNA	2.91
8	PP2A	3.27
9	proteasome	3.58
10	HSP90	4.34
11	HDAC	4.84
12	RNA	5.43
13	protein	5.74
14	ctrl	5.89
15	TOP2 cat	8.41

3-ATA Rank	Class	Score
1	DNA	1.56
2	ionophore	2.85
3	RNA	4.11
4	V-ATPase	4.24
5	ctrl	4.35
6	Eg5	4.94
7	actin	4.97
8	HSP90	5.52
9	protein	5.62
10	proteasome	5.81
11	tubulin	6.47
12	HDAC	7.29
13	HSP60	7.64
14	PP2A	9.80
15	TOP2 cat	11.96

resveratrol Rank	Class	Score
1	DNA	0.92
2	RNA	2.75
3	ionophore	2.87
4	actin	3.90
5	V-ATPase	3.97
6	HSP90	4.30
7	ctrl	4.37
8	proteasome	4.48
9	Eg5	4.63
10	protein	4.92
11	HSP60	5.38
12	tubulin	6.41
13	HDAC	6.89
14	TOP2 cat	6.98
15	PP2A	9.42

Figure 5. Target Profiling of Rotenone, 3-ATA, and Resveratrol by Using Morphobase

src^{ts}-NRK and HeLa cells were treated with rotenone, 3-ATA, or resveratrol, and the obtained phenotype multiparameters were subjected to Morphobase analysis. Target prediction was carried out based on probability scores and similarity ranks, determined by Euclidean distance metrics.

(A) PCA scores of rotenone, 3-ATA, and resveratrol were projected onto 2D scatterplots of PC1 and PC2.

(B) Ranking of the likely modes of action for these compounds among 14 target classes in the training set is shown.

See also Table S3.

phase increased by concentration (Figure S2). Similar results were obtained with the other compounds, suggesting that these active substances affect G2/M phase events.

To detail the mechanism of action of these compounds, we performed Morphobase profiling. Following treatment with NPD6689, NPD8617, and NPD8969 at the concentrations in Table S1, nuclei were stained, and the resulting morphological changes were quantified by IN Cell Analyzer. The obtained phenotypic multiparameters were compared with the reference data set and subjected to statistical analysis. On projecting the samples' PCA scores, the phenotypic responses of NPD6689, NPD8617, and NPD8969 were similar to each other and formed a cluster around tubulin inhibitors in the scatterplots (Figure 6A). In addition, based on the similarity analysis, NPD6689 was predicted to perturb microtubule dynamics ($Score_{tubulin}$ = 1.06), and most of its 20 closest neighbors were typical microtubule inhibitors (Figure 6B; Table S4). Similar results were obtained for NPD8617 and NPD8969, indicating that the molecular target of these compounds is the microtubule system.

To verify these predictions, the compounds were subjected to proteome profiling. The proteomic variation of 296 spots that matched on all gel images was quantified, and hierarchical cluster analysis was performed as described (Muroi et al., 2010). Consistent with the Morphobase profiling, they were clustered with typical microtubule-targeting inhibitors and near the TOP2 catalytic inhibitors, such as BNS22 and ICRF193 (Figure S3).

The mechanism of action with regard to the microtubule system was confirmed by in vitro microtubule assembly assay. All three compounds inhibited the polymerization of tubulin dose dependently (Figures 6C and S4A). Furthermore, these effects were visualized in intact cells by immunofluorescence.

Table 1. Growth Inhibitory Effects of NPD6689, NPD8617, and NPD8969 in Various Cancer Cell Lines

	IC_{50} (μM)		
Cell Line	NPD6689	NPD8617	NPD8969
A549	1.7	0.4	1.1
HeLa	0.6	0.2	0.2
HL-60	1.7	0.2	1.6
HT1080	2.0	0.2	0.5
Jurkat	0.6	0.1	0.2
MG-63	0.9	0.2	0.5
Saos-2	2.7	0.3	2.1
src^{ts}-NRK	4.1	0.7	0.7

See also Figure S2.

After a 12 hr treatment, NPD6689 and NPD8617/NPD8969 effected microtubule depolymerization, causing short microtubule fragments to scatter throughout the cytoplasm as vinblastine treatment (Figures 6D and S4B). The effects that approximated those of TOP2 catalytic inhibitors were excluded due to the lack of distorted spindles and the failure of chromosomal alignment and segregation. These data suggest that NPD6689, NPD8617, and NPD8969 inhibit microtubule integrity in cell-free and cell-based systems.

DISCUSSION

The discovery of novel bioactive substances has become routine; however, one must judge immediately if their activities in a primary screening can be advanced to the drug development stage. Thus, the approximate mode of action must be determined to select the compounds that selectively attack tumors, and the speed of identification will save time and avoid unnecessary efforts from being made. It has been known that experienced cell biologists can judge the presumed mechanism of action of a test compound properly by the simple observation of typical morphological changes in treated cells. So far, several morphology-based assay systems, using mammalian cells, filamentous fungi, and yeasts, have been developed, some of which have successfully led to the discovery of unique drugs and probes (Frost et al., 1995; Gunji et al., 1983). In addition, the accumulated knowledge on phenotypic data can help us avoid the same mistakes repeatedly. For instance, we have developed an in-house phenotype evaluation system, using K562 cells (Osada et al., 1988), HL-60 cells, SHSY-5Y cells, tsFT210 cells (Osada et al., 1997), and *src*^{ts}-NRK cells, which was effectively utilized for the discovery of novel microbial metabolites (Kakeya et al., 1995) and to discriminate typical ones: PKC inhibitors, such as staurosporine and K252a (blebbing in K562 cells); tumor promoters, such as teleocidins and TPA (differentiation of HL-60 cells; Huberman and Callaham, 1979); and protein synthesis inhibitors (flat reversion of *src*^{ts}-NRK cells; Osada et al., 1991). However, such know-how is just empirical—there is obvious lack of consensus on morphological changes, partly due to a skill shortage, interobserver variability, and the differences of the cell lines and test compounds between laboratories—which often leads to inconclusive results and delays in the wide application of this method.

While screening for a compound that reverts the morphology of *src*^{ts}-NRK cells, we observed that vinblastine induced a notable phenotype (Figure 1). We also noticed that when treated with other chemicals, these cells experienced an endless variety of changes in shape, prompting us to record the phenotypes of *src*^{ts}-NRK cells that were induced by various compounds and classify these changes by certain rules. As expected, the cytoskeletal modulators of tubulin and actin dynamics induced characteristic morphological changes that were associated with their respective targets. Notably, the other drugs, such as inhibitors of macromolecule synthesis, HSP, or HDAC inhibitors, whose effects are unrelated to the cytoskeleton, also induced the unique alternations in morphology. The cross-validation of phenotypic responses between *src*^{ts}-NRK and HeLa cells has the following advantage: for either cell line, it was difficult to recognize certain phenotypes, such as those induced by HDAC and proteasome inhibitors in *src*^{ts}-NRK cells (flattened), and protein or RNA synthesis inhibitors in HeLa cells (toxic/growth inhibition). However, with phenotype response data for two distinct cell lines, we could discriminate them easily. Another advantage is the increase in number of compounds that can be analyzed; because drug sensitivity depends on cell types, by using two different cell lines, we could validate the phenotype of a drug that could not be visualized in either cell line in individual assays. Finally, we could easily discern the 13 types of phenotypes that were induced by typical anticancer drugs (Figure 1). Few studies have reported the systematic collection of the morphological changes that are induced by drugs in intact mammalian cells or their chemical-genetic classification (Sumiya et al., 2011), due to the limited number of phenotypic changes observed in the cells used. Our observations on the *src*^{ts}-NRK cell line revealed their potential to react to external signals with a wide variety of the morphological changes, possibly because it was transformed by oncogenic *v*-Src (Chen et al., 1977). Compared with HeLa cells, the broad spectrum of Src activities (Thomas and Brugge, 1997) might confer specific characteristics in a highly developed cytoskeletal system, enhance survival in a specific environment and against cytocidal drugs, or disrupt inherent cell-cycle checkpoints. Thus, we expect the ability to induce these changes to be coupled with many diverse classes of cellular targets. Dozens of Src-interacting proteins have been identified (Luo et al., 2008); however, the precious role of Src and the impact of its modulators on morphology remain unclear. Agents that induce unique shapes in *src*^{ts}-NRK cells are potentially useful drugs for cancer treatment or probes for better understanding of Src function and its related signal transduction.

In this report, we developed a high-content image method and a phenotype profiling system using a similarity search software, based on a statistical analysis of multiparametric phenotype responses, to identify the molecular targets of compounds of interest with an "unbiased eye." Unlike other methods (Pepperkok and Ellenberg, 2006), our system consists only of a 96-well plate, a microscope, and general fluorescent nuclear staining. Thus, this simple system allows us to select substances immediately without the pitfalls of fluorescence-based assays. Actually, in Morphobase profiling, we can distinguish between the modes

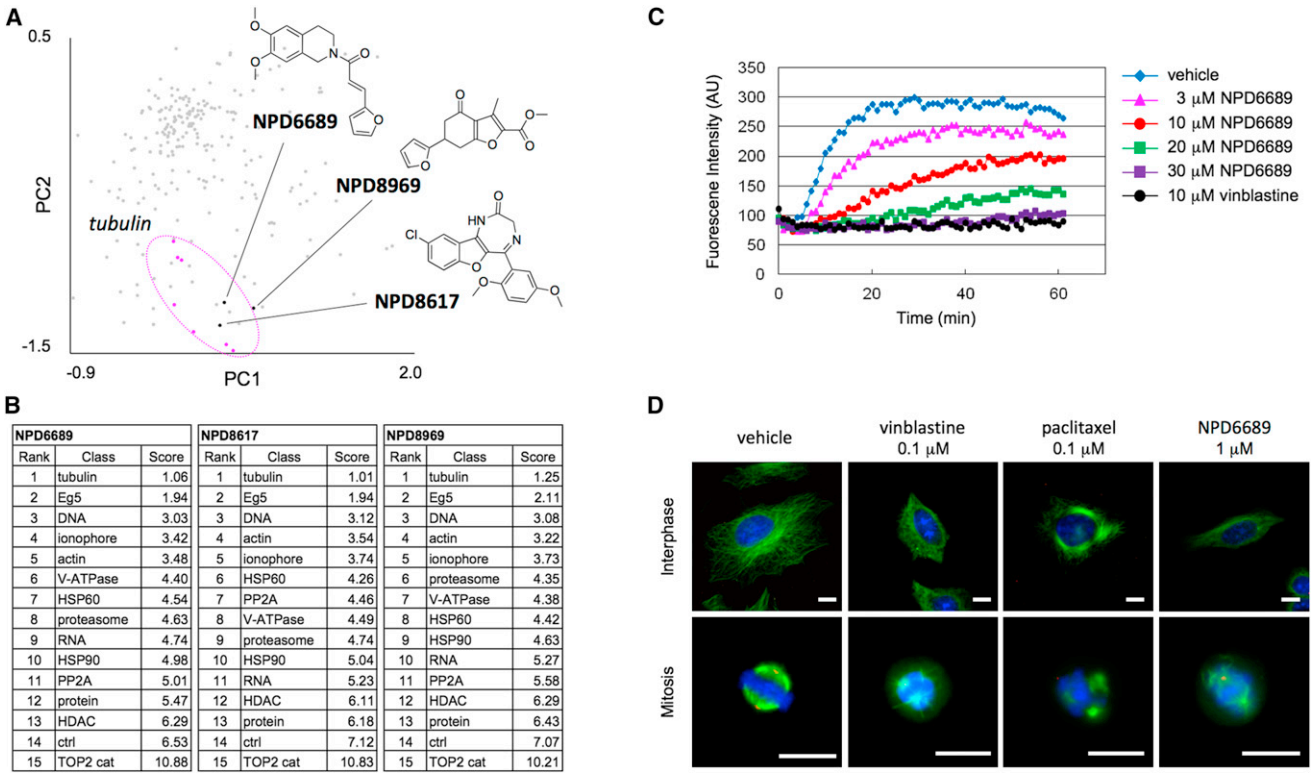

B

NPD6689		
Rank	Class	Score
1	tubulin	1.06
2	Eg5	1.94
3	DNA	3.03
4	ionophore	3.42
5	actin	3.48
6	V-ATPase	4.40
7	HSP60	4.54
8	proteasome	4.63
9	RNA	4.74
10	HSP90	4.98
11	PP2A	5.01
12	protein	5.47
13	HDAC	6.29
14	ctrl	6.53
15	TOP2 cat	10.88

NPD8617		
Rank	Class	Score
1	tubulin	1.01
2	Eg5	1.94
3	DNA	3.12
4	actin	3.54
5	ionophore	3.74
6	HSP60	4.26
7	PP2A	4.46
8	V-ATPase	4.49
9	proteasome	4.74
10	HSP90	5.04
11	RNA	5.23
12	HDAC	6.11
13	protein	6.18
14	ctrl	7.12
15	TOP2 cat	10.83

NPD8969		
Rank	Class	Score
1	tubulin	1.25
2	Eg5	2.11
3	DNA	3.08
4	actin	3.22
5	ionophore	3.73
6	proteasome	4.35
7	V-ATPase	4.38
8	HSP60	4.42
9	HSP90	4.63
10	RNA	5.27
11	PP2A	5.58
12	HDAC	6.29
13	protein	6.43
14	ctrl	7.07
15	TOP2 cat	10.21

Figure 6. Target Profiling of Three Antimitotics by Using Morphobase

src^{ts}-NRK and HeLa cells were treated with NPD6689, NPD8617, or NPD8969, and the resulting phenotype multiparameters were subjected to Morphobase analysis.

(A) PCA scores for NPD6689, NPD8617, and NPD8969 were projected onto a 2D scatterplot of PC1 and PC2.

(B) Ranking of the likely mode of action among 14 target classes in the training set is shown.

(C) Effect of NPD6689 on in vitro tubulin polymerization is presented.

(D) Effect of NPD6689 on microtubules in interphase and mitotic spindle morphology is demonstrated. Cells were treated with the indicated compounds for 12 hr and stained with anti-α-tubulin (green), anti-γ-tubulin (red), and DAPI (blue). Scale bars, 10 μm.

See also Figures S2–S5 and Table S4.

of action of BNS22 and ICRF193 (TOP2 catalytic inhibitors) and etoposide (TOP2 poison), although they target the same protein, as in proteome profiling. Intriguingly, proteasome and HSP90 inhibitors or TOP2 catalytic and tubulin inhibitors lay in overlapping clusters by proteome profiling, but Morphobase profiling discriminated them clearly. Nonetheless, Morphobase suffers from a disadvantage in characterizing drugs that effect colorless morphological change, such as certain kinase inhibitors. Thus, an effective complementary combination of proteome and Morphobase profiling should be required to identify the mechanism of action more accurately.

Morphobase profiling provides us an exciting perspective for the prediction of the side effects and ancillary mechanisms of a drug. Recently, we focused on rotenone, 3-ATA, and resveratrol and identified their additional modes of action, consist with previous reports: rotenone as a tubulin inhibitor (Brinkley et al., 1974) and the latter two drugs as DNA synthesis inhibitors (Diccianni et al., 2004; Leone et al., 2010). Further characterization of the compounds that we examined in this study and those in widespread clinical practice will increase our understanding of their action mechanisms and side effects, advancing drug discovery efforts. On the contrary, drug-induced phenotypes are often changed depending on its concentration, and Morphobase mostly provided the responsible target for its growth inhibitory activity. In our future study, the assessments in primary screening will be carried out at single concentration in order to select compounds of interest from huge samples as quick as possible. Consequently, to speculate on a target, we will examine candidates' biological activities at multiple concentrations at first and then we turn into the morphological profiles.

More recently, we have identified a biosynthetic gene cluster for terpendole E and isolated several indole-alkaloid compounds from the gene-engineered strain of *Chaunopycnis alba* (Motoyama et al., 2012). Paspaline is a common key intermediate of the terpendole pathway and paxilline pathway. The molecular target of paspaline isolated from the mutant strain of *C. alba* is predicted to be Eg5 by Morphobase profiling (Figures 4 and S6A). Remarkably, the target can be predicted, even when crude extracts of the mutant strain (PQ-2) were tested (Figures S6B and 6C). These data verified the utility of our profiling system to predict various pharmacological targets of mechanistically unknown drugs and even crude natural products.

In conclusion, to discover small drug-like molecules, we developed a cell phenotype profiling system using a morphology

database, Morphobase. Our system classifies the modes of action of test compounds and predicts side and off-target effects, leading us to identify NPD6689, NPD8617, and NPD8969 as tubulin inhibitors. Currently, there are many cancer therapeutics that alter microtubule dynamics, including vinca alkaloids and taxanes. Tubulin is an old molecular target, but it remains attractive, as demonstrated by the recent FDA approval of eribulin for cancer treatment (Jain and Cigler, 2012). Although 6-furan-2-yl-3-methyl-4-oxo-4,5,6,7-tetrahydro-1*H*-indole-2-carboxylic acid derivatives that have similar chemical structures to NPD8969 have been reported as tubulin inhibitors (Screpanti et al., 2010), others are structurally unrelated to existing antitubulin agents. In addition, these antimitotics have antiproliferative activities against the vindesine- and paclitaxel-resistant H69 human small-cell lung cancer cell line (Figure S5), implicating it as a lead compound for the development of a new class of antitubulin drugs that overcome clinically evident drug resistance.

The Morphobase system rapidly groups a newly discovered compound to a class with similar mechanisms of action. With data on other cell lines, the exact molecular target can be pinpointed, based on the combination of morphological changes. Knockdown of specific genes by RNAi might provide us with exact morphological changes in the cells and improve the accuracy of the system in identifying the molecular mechanisms of drug activity and toxicity as well.

SIGNIFICANCE

To discover small drug-like molecules, we established the encyclopedic cell morphology database Morphobase, being inspired by our findings that cells dynamically and specifically alter their morphology depending on the mode of action of a drug. We examined the effects of approximately 200 well-characterized drugs on the morphological changes of intact cells in two cancer cell lines. We also prepared a custom-made image analysis algorithm to monitor cell morphology in detail and transformed an analog cell morphology database into an automated high-content database in which the phenotypes and mechanism of action of a drug are quantitatively linked in a chemical-genetic fashion. Using this database, we can easily discriminate typical anticancer drug-induced phenotypes and profile the side effects of drugs with multiple biological targets, such as rotenone. Moreover, in combination with statistic computations, we identified tubulin as the molecular target of the mechanistically unknown drugs NPD6689, NPD8617, and NPD8969 and demonstrated that these compounds inhibit microtubule dynamics in vitro and in a cell-based system.

Overall, as an alternative to current high-content approaches, we established a chemical-genetic phenotype profiling system, based on Morphobase. Our system classifies the modes of action of well-characterized compounds and predicts compounds with reported side (or off-target) effects or with unknown mechanisms. This sensitive and convenient profiling tool can determine the mechanisms of action and off-target effects of drugs and will facilitate the discovery of bioactive compounds with unknown mechanisms of action.

EXPERIMENTAL PROCEDURES

Compounds

Authentic compounds and the chemical library were provided by the RIKEN NPDepo (Osada, 2010) and SCADS inhibitor kits (Kong et al., 2010). The origins of all compounds used to construct Morphobase are summarized in Table S1. The purity and structure of each hit compound were confirmed by spectral analysis; only NPD6689, due to its low purity, was prepared by chemical synthesis (see also Supplemental Experimental Procedures).

Cell Culture

src^{ts}-NRK cells (Chen et al., 1977), rat kidney cells that were infected with ts25, a T class mutant of Rous sarcoma virus Prague strain (gifted from Dr. Y. Uehara), were cultured at permissive temperature (32°C) in Eagle's minimal essential medium (EMEM; Sigma-Aldrich), supplemented with 10% calf serum (CS; Nichirei). The human cervix epidermoid carcinoma cell line HeLa, the human fibrosarcoma cell line HT1080, and the human lung adenocarcinoma cell line A549 were cultured in Dulbecco's modified Eagle's medium (DMEM; Invitrogen), supplemented with 10% fetal bovine serum (FBS, Nichirei). The human small-cell lung cancer cell line H69, vindesine-resistant (H69/VDS) and paclitaxel-resistant cell lines (H69/Txl) (gifted from Dr. F. Koizumi) (Yoshida et al., 2007), the human promyelocytic leukemia cell line HL-60, and the human T lymphocyte cell line Jurkat were cultured in RPMI-1640 medium (Invitrogen), supplemented with 10% FBS. The human osteosarcoma cell line MG-63 was cultured in EMEM, supplemented with 10% FBS. The human osteosarcoma cell line Saos-2 was cultured in McCoy's (Invitrogen), supplemented with 10% FBS. All cell lines except for *src*^{ts}-NRK and H69 were obtained from RIKEN Cell Bank.

Image Acquisition and Analysis

src^{ts}-NRK cells (1×10^4 cells/well in 100 μl EMEM) and HeLa cells (4×10^3 cells/well in 100 μl DMEM) were plated on poly-D-lysin-coated, black, 96-well clear-bottom plates (Bio-One μclear; Greiner). After a 48 or 24 hr exposure to a test compound for *src*^{ts}-NRK or HeLa cells, respectively, the cells were fixed by direct addition of 100 μl 7.4% formalin and 2 μg/ml Hoechst 33342 (Sigma-Aldrich) in PBS and were incubated for 1 hr at room temperature. Bright-field images and corresponding nuclear images were acquired on an IN Cell Analyzer 2000 (GE Healthcare) using a ×40 objective (NA 0.45), a 12-bit camera with 1 × 1 pixel binning, and a laser autofocus system until 1,500 cells were analyzed in each well. Unanalyzable images—such as those with a tiny scratch on the plates or floc—were removed, and the remaining images, consisting of approximately 1,000 cells, were analyzed with custom-designed image analysis algorithms that were created with IN Cell Developer Toolbox as follows:

Step 1: "Nuclear" segmentation. Nuclear-stained images were segmented using the objective segmentation module. Postprocessing nodes, such as dilation, erosion, and sieve, were used to separate close nuclei and properly segment the diverse nuclear phenotypes.
Step 2: "Cell" segmentation. First, preprocessing (inversion of intensity of bright-field images) and removal of tiny objects that were irrelevant to cell shape were performed. Then, "Cell center" was predefined as a seed region of cell contour using the objective segmentation module and postprocessing nodes and allocating nuclei to respective cells. "Cell" was defined as the cellular regions that corresponded to "Cell center" by the objective segmentation module.
Step 3: Granular segmentation. The invert images above and pseudofluorescence images that were generated from bright-field images were used to detect textures, such as granules and vesicles, which were recognized by the vesicle segmentation module.
Step 4: Measure nodes. After individual cells were segmented, 12 user-defined descriptors (nuclear area, nuclear perimeter, nuclear form factor, nuclear major/minor axis length, nuclear count, nuclear intensity, cell area, cell perimeter, cell major/minor axis length, cell form factor, granular counts, and granular area) were calculated for each cell.

Statistical Analysis

Data Processing, Normalization, and PCA

To characterize well-level phenotypic responses, the average, median, and SD of each parametric measurement were calculated. Because the median

nuclear count of HeLa cells was constant (i.e., 1) regardless of treatment, 71 parameters (12 parameters × 3 statistics × 2 cells − 1 statistics) were normalized to the average corresponding control values of the DMSO-treated cells; common logarithmic outputs (x_j) were then applied to the subsequent statistical analysis. For PCA, The eigenvalue-eigenvector of the covariance matrix was calculated, and the resulting principal component scores were displayed in a 2D scatterplot.

Target Estimation by Morphobase Profiling

The prediction of a target molecule or mechanism of action of a test drug was demonstrated by using two statistical computations:

(1) Probability scores. First, we calculated the coordinate of the median point ($a_i = (a_{i1}, a_{i2} \ldots a_{in})$) and the SD ($s_i = (s_{i1}, s_{i2} \ldots s_{in})$) for each well-characterized "*Target*$_i$" as a training data set. To predict a compound's mechanism of action, a parameter, termed "probability score," was derived, according to

$$Score_i = \sqrt{\frac{\sum_{j=1}^{n}\left(\frac{x_j - a_{ij}}{s_{ij}}\right)^2}{n}},$$

where x_j is the coordinate of the test compound, and n is the number of the parameter. If $Score_i = 0$, the compound lies at the median point of *Target*$_i$. If probability $Score_i = 1$, it lies on the hyperplane that forms from the median point and SD of *Target*$_i$: A smaller score reflects a greater probability.

(2) The ranking of the nearest neighbors to a test compound. The similarity is determined by Euclidean distance between selected compound and reference compounds: smaller distance reflects closer phenotypic readouts to the test compound. We can assign test compound to the class to which most of its nearest neighbors belong.

In Vitro Tubulin Polymerization Assay

In vitro tubulin polymerization assay was performed using the Tubulin Polymerization Assay Kit (Cytoskeleton) per the manufacturer's instructions. Briefly, lyophilized porcine tubulin was solubilized to a final concentration of 2 mg/ml in reaction buffer, containing 80 mM PIPES (pH 6.9), 2 mM $MgCl_2$, 0.5 mM EGTA, 1 mM GTP, 10 μM fluorescent reporter, and 20% glycerol, and kept at 4°C. Compounds, (100 × DMSO stock solutions) were added to prewarmed half-area 96-well black plates. Cold tubulin solution was added to the wells, the plate contents were mixed by shaking, and the absorbance at 340 nm was read every minute for 1 hr.

Immunofluorescence Cell Staining

For α-tubulin and γ-tubulin costaining, cells were fixed in ice-cold methanol for 5 min and washed with PBS. After being blocked with 0.5% BSA in PBS for 5 min at room temperature, the slides were incubated sequentially with primary antibodies, each diluted 1:200 in PBS with 0.5% BSA, for 1 hr at 37°C and Alexa-conjugated secondary antibodies, each diluted 1:500 in PBS with 0.5% BSA, for 40 min at 37°C. Cells were also counterstained with DAPI to visualize the nuclei. Images were acquired on a fluorescence microscope (PROVIS AX70; Olympus). The primary antibodies were mouse monoclonal anti-α-tubulin and rabbit polyclonal anti-γ-tubulin (Sigma-Aldrich); the secondary antibodies were Alexa 488 goat anti-mouse IgG and Alexa 546 goat anti-rabbit IgG (Molecular Probes).

SUPPLEMENTAL INFORMATION

Supplemental Information includes six figures, four tables, and Supplemental Experimental Procedures and can be found with this article online at http://dx.doi.org/10.1016/j.chembiol.2012.10.014.

ACKNOWLEDGMENTS

We thank Y. Uehara (Iwate Medical University) for kindly providing *src*^{ts}-NRK cells, F. Koizumi (National Cancer Center Research Institute) for providing H69, H69/VDS, and H69/Txl cells, J. Kobayashi (Hokkaido University) for providing iejimalide A, and H. Nakamura (Gakushuin University) for providing GN26361 and mizoribine. The SCADS inhibitor kits were a kind gift of the Screening Committee of Anticancer Drugs supported by a Grant-in-Aid for Scientific Research on Innovative Areas, Scientific Support Programs for Cancer Research from MEXT. We also thank H. Aono, Y. Fukushima, K. Noda, and H. Kondo for technical assistance, K. Wierzba and T. Motoyama for critical review of the manuscript, and members of RIKEN NPDepo for the chemical libraries. This work was supported in part by a Special Postdoctoral Research Program of RIKEN, Grant-in-Aid for Scientific Research (KAKENHI), Health and Labour Sciences Research Grant, and the Program for Promotion of Basic and Applied Researches for Innovations in Bio-oriented Industry.

Received: July 18, 2012
Revised: October 19, 2012
Accepted: October 23, 2012
Published: December 20, 2012

REFERENCES

Abassi, Y.A., Xi, B., Zhang, W., Ye, P., Kirstein, S.L., Gaylord, M.R., Feinstein, S.C., Wang, X., and Xu, X. (2009). Kinetic cell-based morphological screening: prediction of mechanism of compound action and off-target effects. Chem. Biol. *16*, 712–723.

Brinkley, B.R., Barham, S.S., Barranco, S.C., and Fuller, G.M. (1974). Rotenone inhibition of spindle microtubule assembly in mammalian cells. Exp. Cell Res. *85*, 41–46.

Chen, Y.C., Hayman, M.J., and Vogt, P.K. (1977). Properties of mammalian cells transformed by temperature-sensitive mutants of avian sarcoma virus. Cell *11*, 513–521.

Diccianni, M.B., Yu, J., Meppelink, G., de Vries, M., Shao, L., Gebauer, S., Shih, H., Roberts, W., Kilcoin, N.P., Pullen, J., et al. (2004). 3-amino thioacridone inhibits DNA synthesis and induce DNA damage in T-cell acute lymphoblastic leukemia (T-ALL) in a p16-dependent manner. J. Exp. Ther. Oncol. *4*, 223–237.

Feng, Y., Mitchison, T.J., Bender, A., Young, D.W., and Tallarico, J.A. (2009). Multi-parameter phenotypic profiling: using cellular effects to characterize small-molecule compounds. Nat. Rev. Drug Discov. *8*, 567–578.

Fenteany, G., Standaert, R.F., Lane, W.S., Choi, S., Corey, E.J., and Schreiber, S.L. (1995). Inhibition of proteasome activities and subunit-specific amino-terminal threonine modification by lactacystin. Science *268*, 726–731.

Frémont, L. (2000). Biological effects of resveratrol. Life Sci. *66*, 663–673.

Frost, D.J., Brandt, K.D., Cugier, D., and Goldman, R. (1995). A whole-cell *Candida albicans* assay for the detection of inhibitors towards fungal cell wall synthesis and assembly. J. Antibiot. (Tokyo) *48*, 306–310.

Gunji, S., Arima, K., and Beppu, T. (1983). Screening of antifungal antibiotics according to activities inducing morphological abnormalities. Agric. Biol. Chem. *47*, 2061–2069.

Houle, D., Govindaraju, D.R., and Omholt, S. (2010). Phenomics: the next challenge. Nat. Rev. Genet. *11*, 855–866.

Huberman, E., and Callaham, M.F. (1979). Induction of terminal differentiation in human promyelocytic leukemia cells by tumor-promoting agents. Proc. Natl. Acad. Sci. USA *76*, 1293–1297.

Jain, S., and Cigler, T. (2012). Eribulin mesylate in the treatment of metastatic breast cancer. Biologics *6*, 21–29.

Kakeya, H., Takahashi, I., Okada, G., Isono, K., and Osada, H. (1995). Epolactaene, a novel neuritogenic compound in human neuroblastoma cells, produced by a marine fungus. J. Antibiot. (Tokyo) *48*, 733–735.

Kawatani, M., Takayama, H., Muroi, M., Kimura, S., Maekawa, T., and Osada, H. (2011). Identification of a small-molecule inhibitor of DNA topoisomerase II by proteomic profiling. Chem. Biol. *18*, 743–751.

Kong, D., Yamazaki, K., and Yamori, T. (2010). Discovery of phosphatidylinositol 3-kinase inhibitory compounds from the Screening Committee of Anticancer Drugs (SCADS) library. Biol. Pharm. Bull. *33*, 1600–1604.

Kubo, A., Nakagawa, K., Varma, R.K., Conrad, N.K., Cheng, J.Q., Lee, W.C., Testa, J.R., Johnson, B.E., Kaye, F.J., and Kelley, M.J. (1999). The p16

status of tumor cell lines identifies small molecule inhibitors specific for cyclin-dependent kinase 4. Clin. Cancer Res. *5*, 4279–4286.

Leone, S., Cornetta, T., Basso, E., and Cozzi, R. (2010). Resveratrol induces DNA double-strand breaks through human topoisomerase II interaction. Cancer Lett. *295*, 167–172.

Luo, W., Slebos, R.J., Hill, S., Li, M., Brábek, J., Amanchy, R., Chaerkady, R., Pandey, A., Ham, A.J., and Hanks, S.K. (2008). Global impact of oncogenic Src on a phosphotyrosine proteome. J. Proteome Res. *7*, 3447–3460.

MacDonald, M.L., Lamerdin, J., Owens, S., Keon, B.H., Bilter, G.K., Shang, Z., Huang, Z., Yu, H., Dias, J., Minami, T., et al. (2006). Identifying off-target effects and hidden phenotypes of drugs in human cells. Nat. Chem. Biol. *2*, 329–337.

Motoyama, T., Hayashi, T., Hirota, H., Ueki, M., and Osada, H. (2012). Terpendole E, a kinesin Eg5 inhibitor, is a key biosynthetic intermediate of indole-diterpenes in the producing fungus *Chaunopycnis alba*. Chem. Biol. *19*, this issue, 1611–1619.

Muroi, M., Kazami, S., Noda, K., Kondo, H., Takayama, H., Kawatani, M., Usui, T., and Osada, H. (2010). Application of proteomic profiling based on 2D-DIGE for classification of compounds according to the mechanism of action. Chem. Biol. *17*, 460–470.

Ohnuki, S., Oka, S., Nogami, S., and Ohya, Y. (2010). High-content, image-based screening for drug targets in yeast. PLoS One *5*, e10177.

Omura, S., Fujimoto, T., Otoguro, K., Matsuzaki, K., Moriguchi, R., Tanaka, H., and Sasaki, Y. (1991). Lactacystin, a novel microbial metabolite, induces neuritogenesis of neuroblastoma cells. J. Antibiot. (Tokyo) *44*, 113–116.

Osada, H. (2010). Introduction of new tools for chemical biology research on microbial metabolites. Biosci. Biotechnol. Biochem. *74*, 1135–1140.

Osada, H., Magae, J., Watanabe, C., and Isono, K. (1988). Rapid screening method for inhibitors of protein kinase C. J. Antibiot. (Tokyo) *41*, 925–931.

Osada, H., Koshino, H., Isono, K., Takahashi, H., and Kawanishi, G. (1991). Reveromycin A, a new antibiotic which inhibits the mitogenic activity of epidermal growth factor. J. Antibiot. (Tokyo) *44*, 259–261.

Osada, H., Cui, C.B., Onose, R., and Hanaoka, F. (1997). Screening of cell cycle inhibitors from microbial metabolites by a bioassay using a mouse cdc2 mutant cell line, tsFT210. Bioorg. Med. Chem. *5*, 193–203.

Pepperkok, R., and Ellenberg, J. (2006). High-throughput fluorescence microscopy for systems biology. Nat. Rev. Mol. Cell Biol. *7*, 690–696.

Perlman, Z.E., Slack, M.D., Feng, Y., Mitchison, T.J., Wu, L.F., and Altschuler, S.J. (2004). Multidimensional drug profiling by automated microscopy. Science *306*, 1194–1198.

Roti, G., and Stegmaier, K. (2012). Genetic and proteomic approaches to identify cancer drug targets. Br. J. Cancer *106*, 254–261.

Screpanti, E., Santaguida, S., Nguyen, T., Silvestri, R., Gussio, R., Musacchio, A., Hamel, E., and De Wulf, P. (2010). A screen for kinetochore-microtubule interaction inhibitors identifies novel antitubulin compounds. PLoS One *5*, e11603.

Sumiya, E., Shimogawa, H., Sasaki, H., Tsutsumi, M., Yoshita, K., Ojika, M., Suenaga, K., and Uesugi, M. (2011). Cell-morphology profiling of a natural product library identifies bisebromoamide and miuraenamide A as actin filament stabilizers. ACS Chem. Biol. *6*, 425–431.

Takahashi, H., Osada, H., Koshino, H., Sasaki, M., Onose, R., Nakakoshi, M., Yoshihama, M., and Isono, K. (1992). Reveromycins, new inhibitors of eukaryotic cell growth. II. Biological activities. J. Antibiot. (Tokyo) *45*, 1414–1419.

Thomas, S.M., and Brugge, J.S. (1997). Cellular functions regulated by Src family kinases. Annu. Rev. Cell Dev. Biol. *13*, 513–609.

Uehara, Y., Hori, M., Takeuchi, T., and Umezawa, H. (1986). Phenotypic change from transformed to normal induced by benzoquinonoid ansamycins accompanies inactivation of p60src in rat kidney cells infected with Rous sarcoma virus. Mol. Cell. Biol. *6*, 2198–2206.

Whitesell, L., Mimnaugh, E.G., De Costa, B., Myers, C.E., and Neckers, L.M. (1994). Inhibition of heat shock protein HSP90-pp60v-src heteroprotein complex formation by benzoquinone ansamycins: essential role for stress proteins in oncogenic transformation. Proc. Natl. Acad. Sci. USA *91*, 8324–8328.

Yoshida, M., Matsui, Y., Ikarashi, Y., Usui, T., Osada, H., and Wakasugi, H. (2007). Antiproliferating activity of the mitotic inhibitor pironetin against vindesine- and paclitaxel-resistant human small cell lung cancer H69 cells. Anticancer Res. *27*, 729–736.

